Theoretical study of porous surfaces derived from graphene and boron nitride

G.S.L. Fabris[a], N.L. Marana[a], E. Longo[b], J.R. Sambrano[a],*

[a] Modeling and Molecular Simulation Group - CDMF, São Paulo State University, P.O. Box 17033-360, Bauru, SP, Brazil
[b] Chemistry Institute - CDMF, Federal University of São Carlos, P.O. Box 14801-907, São Carlos, SP, Brazil

A R T I C L E   I N F O

A B S T R A C T

Porous graphene (PG), graphenylene (GP), inorganic graphenylene (IGP-BN), and porous boron nitride (PBN) single-layer have been studied via periodic density functional theory with a modified B3LYP functional and an all-electron Gaussian basis set. The structural, elastic, electronic, vibrational, and topological properties of the surfaces were investigated. The analysis showed that all porous structures had a nonzero band gap, and only PG exhibited a non-planar shape. All porous structures seem to be more susceptible to longitudinal deformation than their pristine counterparts, and GP exhibits a higher strength than graphene in the transversal direction. In addition, the electron densities of GP and IGP-BN are localized closer to the atoms, in contrast with PG and PBN, whose charge density is shifted towards the pore center; this property could find application in various fields, such as gas adsorption.

1. Introduction

The interest in graphene-based systems with a honeycomb network has considerably increased, owing to their huge scientific and technological potential in material science and their possible applications in nanodevices [1,2], supercapacitors [3], theranostics [4], immunotherapy [5], and fuel cells [6]. Particular attention has been extended to inorganic graphene analogues, such as hexagonal boron nitride (hBN) [7], with a lattice parameters [8] mismatch of ~1.8%, relative to graphene. Similar to graphene, hBN can exist in several allotropes, such as nanotubes [9], fullerenes [10], and nanoscrolls [11].

Graphene is a zero-gap material, which limits its application in electronic devices. Consequently, developing approaches aimed at modifying the material in such a way to remove this band gap limitation has attracted considerable attention. Different chemical methods can be used to modify the band gap, such as atomic adsorption [12], fluorination [13], oxidation [14], and hydrogenation [15], as well as physical methods such as strain [16] and the introduction of defects [17] by doping [18] and/or structural modifications.

In the past years, other kinds of 2D structures have also attracted attention, such as porous graphene (PG) [19,20]. Even though PG retains a hexagonal structure similar to that of graphene, this material has a wide band gap, as theoretically reported by Du et al. [21]. Using plane-wave density functional theory (DFT) calculations, they obtained band gaps of 2.36 and 3.20 eV with LDA and HSE06 functionals, respectively. Later on, Ding et al. [22] obtained a band gap of 2.35 eV using the same methodology with a LDA functional; however, it is well known that the LDA exchange-correlation functional underestimates the band gap energy.

In 2012, Brunetto et al. [23] reported a theoretical study of a structure known as biphenylene carbon or graphenylene (GP), using the density functional tight-binding [24] method. They showed that in the basis of ab initio calculations, the selective removal of hydrogens atoms from the PG triggers a spontaneous conversion of the structure to a GP sheet, and that the band gaps of PG and GP are 3.3 and 0.8 eV, respectively. Recently Yu [25] showed that GP has a promising potential as anode material for lithium-ion batteries and exhibits high storage capabilities; in addition, Song et al. [26] reported that GP, with its well-defined porous network, can be used as molecular sieve for gas separation and storage. Recently GP was obtained experimentally [27,28] through a different route than that theoretically described by Brunetto's work.

Using plane-wave DFT calculations, a few years ago Ding and coworkers [22] proposed a PG analogue, porous boron nitride (PBN), with a band gap of 4.27 eV. Later on, Perim and coworkers [29] introduced a GP analogue, inorganic graphenylene (IGP-BN), using a DFT approach based on localized wave functions and the PBE functional. They reported band gaps of 4.57 and 4.14 eV for the PBN and IGP-BN structures, respectively.

The theoretical studies mentioned above have focused only on evaluating the structural parameters and band gaps of the materials investigated. Prompted by the need to understand and obtain accurate predictions of other important properties, here we carried out periodic DFT simulations to determine the structural, electronic, elastic, and vibrational properties of the PG, GP, PBN, and IGP-BN materials. To the best of our knowledge, no previous computational studies of the elastic and vibrational properties of these porous 2D systems at this level of theory have been published. Moreover, we present the first application of the analysis of bond critical points (BCPs) to explore chemical interactions in solid-state systems by the quantum theory of atoms in molecules (QTAIM) [30,31].

2. Computational methods and modeled systems

All present calculations were performed using the periodic DFT approach, as implemented in the CRYSTAL14 [32] software. Owing to the importance of the choice of the appropriate functional for the quality of the structural and electronic results, seven functional have been selected for comparison: BLYP, B3LYP, PBE, PBE0, PBESOL0, HSE06, and the modified B3LYP* (12% hybrid) functional. The description of these functionals can be found in the CRYSTAL14 manual and references [33]. The hybrid percentage denotes the fraction of mixing of exact Hartree-Fock (HF) and DFT exchange contributions in the modified functional. The following equation describes the modified B3LYP functional: $E_{xc} = (1-A)\cdot(E_x^{LDA}+0.9\cdot E_x^{BECKE}) + A\cdot E_x^{HF}+0.19\cdot E_c^{LDA}+0.81\cdot E_c^{GGA}$, where A is the hybrid percentage ($A = 0.12$ in the B3LYP* case). The carbon, boron, nitrogen, and hydrogen atoms were described by a triple-zeta plus polarization (TZVP) basis set [34]. Other basis set combinations available in the crystal basis set library (http://www.crystal.unito.it/basis-sets.php) were tested, and the TZVP basis set was chosen because it yielded the most accurate description of the experimental band gap energy and structural parameters of both bulk graphite and hexagonal boron nitride (Table S3), as well as of graphene and single-layer (0001) hexagonal boron nitride (Table S4).

All stationary points were characterized as minima by diagonalizing the Hessian matrix with respect to the unit cell parameters and atomic coordinates, and then analyzing the vibrational modes shown in Tables S1 and S2. The convergence was checked on the gradient components and nuclear displacements, with tolerances on their root mean square set to 0.0001 and 0.0004 a.u., respectively.

The level of accuracy in the evaluation of the infinite Coulomb and HF exchange series is controlled by five parameters α_i, with $i = 1-5$, such that two-electron contributions are neglected when the overlap between atomic functions is below $10^{-\alpha_i}$. In the present calculations, the five α_i parameters have been set to 10, 10, 10, 20, and 40 and the shrinking factor for the Pack-Monkhorst and Gilat nets was set to 20.

The band structure and density of states (DOS) were analyzed using the Properties14 routine implemented in the CRYSTAL code, using the same k-point sampling employed for the diagonalization of the Fock matrix in the optimization process.

The elastic properties were also studied; the elements of the elastic constant tensor (C_{vu}) were calculated using the following equation:

$$C_{vu} = \frac{1}{V}\frac{\partial^2 E}{\partial \eta_v \partial \eta_u}\bigg|_0 \tag{1}$$

where V is the equilibrium unit cell volume, η is the symmetric second-rank pure strain tensor, and the Voigt's notation is adopted. Second derivatives were computed as first numerical derivatives of analytical energy gradients. Owing to the 2D structure of the present systems, the volume can be approximated using the layer thickness and the atomic van der Waals radii.

The electron density was further analyzed by QTAIM, which is a well-established theory providing a quantum description of the probability of electron localization and of the behavior of atoms in a chemical bond. The topological analysis of the electron density can provide important information on the electronic structure, especially of chemical bonds, fundamental to understand the type of interaction between two atoms and the modifications induced by structural rearrangements. The integration of the charge density over the atomic basins gives further information, such as the atomic volume, Bader's atomic charges, and the partitioning of the energy between different atomic contributions. The QTAIM analysis was carried out via the TOPOND program [35] incorporated in CRYSTAL14. Further theoretical details can be found in articles specifically focused on the topological analysis [30,36].

The graphite structure consists of flat layers of carbon atoms linked in a hexagonal shape; in each layer, also known as graphene sheet, the sp²-hybridized carbon atoms are covalently bonded to three other carbon atoms. The space group of graphite is $P6_3/mmc$, with unit cell parameters $a = 2.456$ Å and $c = 6.696$ Å [37].

The structure and lattice parameters of hBN are similar to those of graphite: space group $P-6m2$ and unit cell parameters $a = 2.504$ Å and $c = 6.661$ Å [38]. The graphene and hBN structures are composed of a single-layer in the (0001) direction; graphene has no band gap, whereas the band gap of hBN is 5.96 eV [39].

As a first step for the construction of the porous single-layers structures, the optimization of the lattice parameters and internal coordinates of both bulk graphite and hBN were conducted to minimize the total energy. Then, hBN (0001) single-layer and graphene were built from the optimized bulk structure and reoptimized in function of the internal coordinates. From the results of the structural parameters and band gap, the functional that accurately describes both properties for the bulk and single-layer structures was chosen. In this way, it is expected that the selected functional can ensure that the structural, electronic, mechanical and vibrational properties of the porous structures can be described with a good level of reliability

Fig. 1 shows the structure of PG (Fig. 1a) and PBN (Fig. 1c); both structures were obtained by substituting each atom in the unit cell of their base structures by a benzene-like ring with three hydrogen atoms alternated between carbon atoms. The GP (Fig. 1b) and IGP-BN (Fig. 1d) structures form by spontaneous interconversion of the rings when the hydrogen atoms are removed. These dehydrogenated structures have a higher cohesive energy (E_c) and thus seem to be more stable than the PG and PBN structures, as described in the preliminary reports of Brunetto [23] and Perim [29].

3. Results and discussion

3.1. Structural properties

A full structural optimization of graphite, hBN and their respective (0001) surfaces, graphene and single-layer hBN, were initially carried out using the seven different functionals discussed above, and the results are listed in Table S3 and S4 (Supplementary material).

As can be seen in Table S3, all selected functionals accurately predict the **a** cell parameter of graphite, with virtually no error in the case of the modified B3LYP* functional. Although the calculated **c** parameter is not as accurate as the **a** one, considering the performance of B3LYP and B3LYP* in the simultaneous prediction of both parameters, the B3LYP* functional yields the lowest overall error and is thus the best approximation.

The BLYP and B3LYP functionals yield equally accurate estimates of the **a** parameter of the hBN cell. On the other hand, all functionals overestimate the **c** parameter of hBN. The band gap energies calculated with the B3LYP* functional show the most accurate agreement with the experimental band gap data of hBN.

Based on the above discussion, the B3LYP* functional yields the best description of the cell parameters and band gap energy of both graphite and hBN bulk structures.
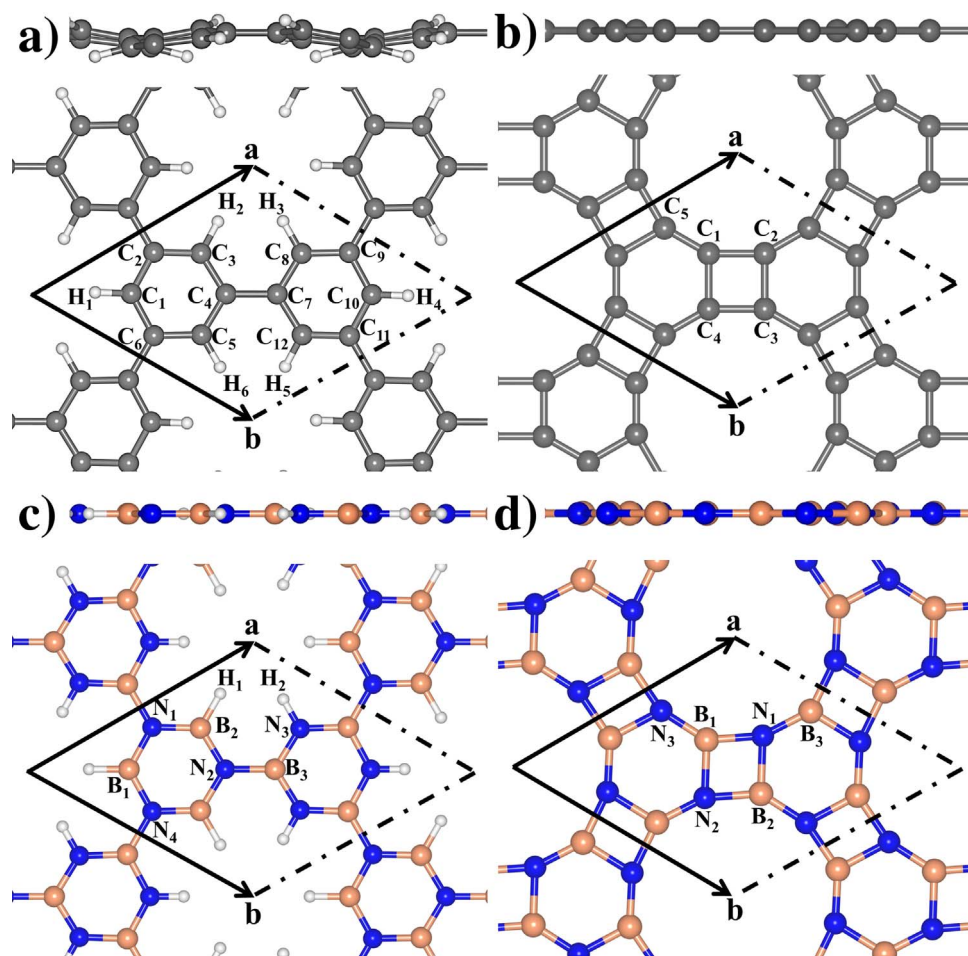
Fig. 1. Side and top view of porous single-layer unit cell of (a) PG, (b) GP, (c) PBN, and (d) IGP-BN, with atom labels also indicated.

Moreover, all functionals were tested on the graphene and single-layer hBN (0001) systems, to confirm that the present theoretical models also provide a reliable description of both surfaces. Table S4 shows the calculated cell parameters and band gap energies of both systems. The analysis of the results in Table S4 confirms that the most accurate structural parameters and band gap for graphene and hBN are once more obtained with the B3LYP* functional and it also produces a C-C and B-N bond lengths of 1.42 and 1.45 Å for graphene and hBN, respectively, in almost exact agreement with the experimental values [40,41]. Also, our group has employed this methodology, and in particular case the hybrid functional B3LYP was successful in describing the properties of other materials [42–46].

It is important to mention that the band gap of bulk hBN has been reported by many experimental and theoretical studies, with different values. For instance, the reported results for the direct or indirect band gap span a very wide range, from 3.6 to 7.1 eV, as reported by Solozhenko et al. [47]. A few ab initio band structure calculations predicted an indirect band gap [48–52] between the M and ~K points, whereas optical measurements indicate a direct band gap [53–55]. Recently, Cassabois [39] and coworkers published an experimental study that trying to solve this long-standing issue, using optical spectroscopy to show that bulk hBN has an indirect band gap of 5.96 eV. The computational framework adopted in the present work also shows an indirect band gap of 5.88 eV between M and ~K points, in accordance with Cassabois.

For comparison purposes, and in absence of relevant experimental information, we decided to maintain the above computational setup also to model the porous structures. As the selected functional and basis sets yield a good description of the precursor structures, they are

also expected to predict the properties of PG, GP, PBN, and IGP-BN with good accuracy, producing reliable and consistent results.

The full optimization procedure shows that the GP, PBN, and IGP-BN keep the hexagonal structure, unlike PG, which shows a 0.01 Å difference between the $\boldsymbol{a}$ and $\boldsymbol{b}$ lattice parameters. Brunetto et al. [23] reported that the space group of PG is C222, but the space groups of the other structures are not reported in the literature. Our simulations show that GP belongs to the P_6/mmm symmetry group with one irreducible atom per unit cell, whereas PBN and IGP-BN belong to the P–$6m$2 space group with six irreducible atoms per unit cell and to the P_6/m space group with two irreducible atoms per unit cell, respectively. The space group of the PG structure, non-planar and with six irreducible atoms per unit cell, is consistent with the previous data reported by Brunetto et al. The calculated lattice parameters, space group, and internal atomic coordinates of all structures are listed in Table S5 (Supplementary Material).

The calculated lattice parameters of PG are a = 7.426 Å and b = 7.437 Å, in good agreement with the reported experimental [19] value of 7.4 Å, whereas the parameters of the GP structure are $a = b = 6.735$ Å. The calculated lattice parameter of PBN, 7.622 Å, is in good agreement with previous theoretical studies [22,29], while $a = b = 6.818$ Å in the case of IGP-BN. Therefore, the GP and IGP-BN structures present a 10% lattice contraction compared with PG and PBN.

The cell parameters, bond lengths, bond angles, and dihedral angles for all studied structures are summarized in Table S6 (Supplementary Material).

In the PG and single-layer PBN systems, the average lengths of intra-ring C_1-C_2 (B_1-N_1) bonds are 1.39 (1.44) Å and those of inter-ring

C_4-C_7 (N_2-B_3) bonds are 1.49 (1.48) Å. The C-H, B-H, and N-H bond lengths are 1.08, 1.19, and 1.01 Å, respectively, whereas the average bond angles centered on C_4, B_3, and N_2 atoms are ~120°. The cyclobutadiene-like unit of GP and IGP-BN is an almost perfect square, with average C_1-C_4, C_1-C_5, B_1-N_3, and B_1-N_2 intra-ring bond lengths of 1.46, 1.35, 1.40, and 1.50 Å, respectively, and average intra-ring bond angles also ~120°. Further information can be found in Table S6 (Supplementary Material).

It is important to observe that PG and PBN have smaller pore diameters (3.73 and 3.92 Å, respectively) compared with GP and IGP-BN, whose pore diameters are 5.47 and 5.51 Å, respectively. These different pore sizes can find application in gas separation and adsorption processes.

In order to investigate the planarity of the surfaces, we modeled in-plane and out-of-plane configurations of the PG and PBN structures. The out-of-plane configuration was the most stable (as confirmed by the absence of negative frequencies) for the PG surface, whereas the in-plane arrangement is the most stable for the PBN surface. On the other hand, the GP and IGP-BN structures are planar, as illustrated by the dihedral angles listed in Table S6 (Supplementary Material).

3.2. Elastic properties

To the best of our knowledge, no experimental or theoretical data on the elastic properties of the present porous surfaces that can be compared with the results of our simulations are available. Our data can thus represent an important reference for future experimental studies.

The calculated elastic constants for graphene and single-layer hBN (which represent the building blocks of the porous structures investigated) were determined in order to verify the numerical accuracy of the modified hybrid functional (B3LYP*) and of the adopted basis set.

In a surface, there are only two elastic constants, labeled C_{11} and C_{12}, which represents the longitudinal compression and transverse expansion of the system, respectively. The calculated elastic constants for graphene (hBN) are C_{11} = 1025.92 (897.58) GPa and C_{12} = 163.01 (188.02) GPa. In order to compare the elastic properties with previous related results, we calculated the Young's modulus (Y) and Poisson coefficients (v), using the following equations: $Y = (C_{11}^2 - C_{12}^2)/C_{11}$ and $v = C_{12}/C_{11}$. The Young's modulus and Poisson coefficient for graphene (hBN) are 1.0 (858.1) TPa and 0.159 (0.209), respectively. These results are in good agreement with the reported experimental values of the Young's modulus (1.0 TPa [56]) and Poisson coefficient (0.165 [57,58]) of graphene, and also with ab initio [59] calculations for hBN.

The good accuracy of the elastic properties calculated for graphene and hBN should ensure an accurate description of the elastic properties of the PG, GP, PBN, and IGP-BN structures, listed in Table 1.

These results show that the longitudinal direction of hBN is more easily deformable than that of graphene, while the transverse direction of graphene is more easily deformable than that of h-BN. Moreover, since hBN has low rigidity, its Poisson coefficient is larger than that of graphene. These observations can assist the prediction of the change in elastic properties upon deposition of graphene on hBN and vice versa.

The C_{11} values in Table 1 also show that the longitudinal direction

of all porous surfaces is more easily deformable compared with the pristine surfaces; moreover, PG is more deformable than PBN, at variance with GP that seems to be more rigid than IGP-BN. PG is more easily deformable than graphene in the transverse direction (based on the C_{12} values), whereas GP is over three times more rigid than PG. The same behavior is observed for the BN-type materials, which thus exhibit a similar trend in the Young's modulus and Poisson coefficients. The higher rigidity of the GP and IGP-BN surfaces could be due to the higher distortion of their atomic network, since the square geometry formed by their atoms has a lower tension than the hydrogenated hexagon of PG and PBN, and in the case of PG the non-planarity has a major influence on the C_{11} constant.

It is important to note that, the mechanical stability of 2D systems requires restrictions on the two elastic constants: $C_{11} > 0$, $C_{11} - C_{12} > 0$ and $C_{11} + 2C_{12} > 0$ [60]. The elastic constants, presented in Table 1, satisfy these restrictions. Also, the C_{11} is larger than C_{12} because the first one is a diagonal component where the stress and strain are applied in the same direction. In C_{12} the stress and strain are applied and induced in different directions. As a general observation, the relative order of the elastic constants is: Diagonal constants, C_{11}, C_{22} and C_{33} are larger than C_{12}, C_{13} and C_{23}, called off-diagonal constants, what are in turn larger than shear, C_{44}, C_{55} and C_{66} constants. Several studies report these behaviors for bulk and surfaces elastic constants [42,61,62].

3.3. Electronic properties

Figs. 2 and 3 display the band structure and density of states of the porous surfaces.

The GP (Fig. 2b) and PBN (Fig. 3a) surfaces have a direct band gap between the top of the valence band (VB) and the bottom of the conduction band (CB), located at the K point. The PG (Fig. 2a) and IGP-BN (Fig. 3b) structures show an indirect band gap between M-K and K points. The PG structure has a wide band gap (3.78 eV) whereas the band gap of GP is 0.83 eV. As shown in the figure, the bands of PG are flat around the top of the VB, which means that the electrons have low mobility in this region; on the other hand, GP shows non-flat bands, indicating a good dispersion, smaller effective mass and a higher mobility for the electrons.

The porosity has a clear impact on the band gap of the graphene-based systems, because the pores are larger than the standards hexagonal units of graphene, suggesting that these materials can be applied in electronic devices, such as transistors [63]. The band gap reduction from PG to GP probably results from the higher structural deformation in the latter when hydrogen atoms are removed, it leads to structural rearrangements, consisting in an alternated rotation (30 degrees) of the hexagonal rings together with a lattice parameter contraction (~10%) which forms a new square ring between the rotated hexagonal rings, as illustrated in Fig. S1 (Supplementary Material), which introduces new virtual energy levels in the forbidden region, associated with the p_z orbitals of the carbon atoms, as can be seen in the density of states (Figs. 2 and 3).

The band gap of PBN, 6.45 eV, is greater than that of hBN, 6.10 eV, and both systems exhibit flat valence and conduction bands. The band gap of IGP-BN decreases to 5.52 eV, which is less than that of the pristine hBN surface, and this system, also exhibits flat bands.

The DOS of PG (Fig. 2a) indicates that the main contribution to the valence and conduction bands around the band gap comes from the $2p_z$ orbital of the carbon atoms, whereas there is no contribution from the $2s$ orbital of the hydrogen atoms. According to Fig. 2b, the main contributor to both valence and conduction bands of GP is the $2p_z$ orbital of the carbon atoms.

In the case of PBN (Fig. 3a), the main contribution to the valence band comes from the $2p_z$ orbital of the nitrogen atoms, with an additional small contribution from the $2p_z$ orbital of boron. The conduction band shows an opposite behavior, with the main contribu-

Table 1
Elastic constants C_{11} and C_{12} (GPa), Young's modulus (Y, GPa), and Poisson coefficients (v).

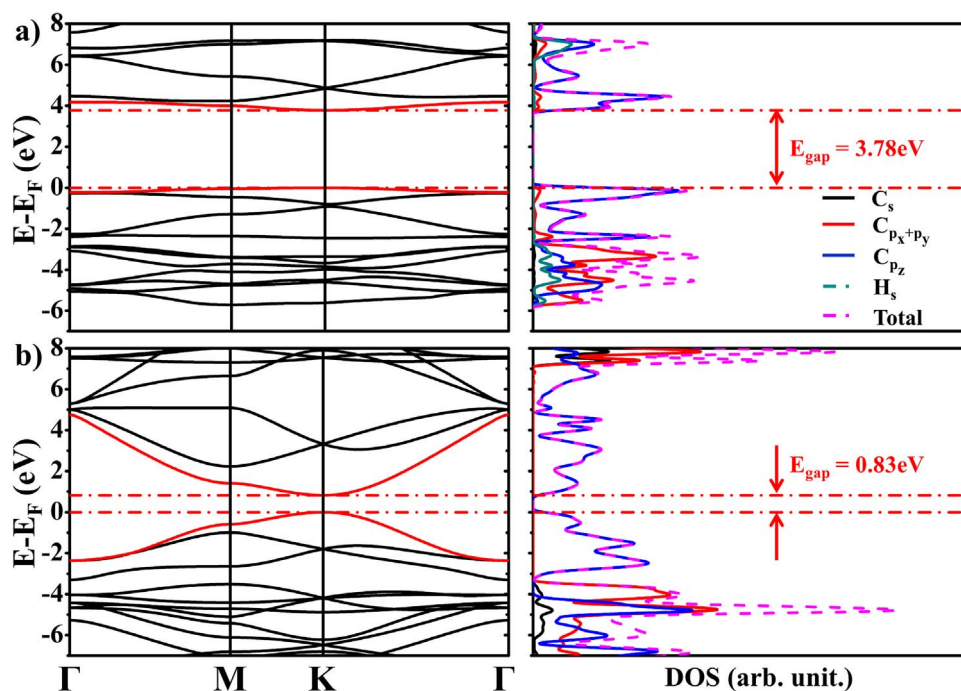|	C_{11}	C_{12}	Y	v
Graphene	1025.92	163.01	1000.02	0.159
PG	304.76	58.45	293.55	0.192
GP	695.44	180.09	648.80	0.259
hBN	897.58	188.02	858.19	0.209
PBN	379.45	109.90	347.62	0.290
IGP-BN	611.09	171.79	562.79	0.281

Fig. 2. Band structure and density of states of (a) PG and (b) GP.

tion close to the band gap region coming from the $2p_z$ orbital of the boron atoms, and with a minor contribution from the $2p_z$ orbital of the nitrogen atoms. The hydrogen atoms do not contribute to the conduction and valence bands around the band gap.

For the IGP-BN (Fig. 3b), the main contribution to the valence and conduction bands comes from the $2p_z$ orbital of the nitrogen and boron atoms, respectively.

3.4. Raman spectra

The Raman vibrational spectra and their most intense modes (without shifts) obtained for graphene, hBN (0001) surface, PG, GP,

PBN, and IGP-BN are displayed in Fig. 4. These spectra provide chemical and structural information useful to interpret the experimental results, as well as a reference fingerprint for the structures. The vibrational frequencies at the Γ point were calculated using the numerical second derivatives of the total energies estimated with the coupled perturbed Hartree-Fock/Kohn-Sham algorithm [64–66].

Graphene exhibits a single Raman-active mode at 1592.92 cm^{-1} (E', carbon symmetric stretching), in agreement with the experimental Raman [67] G band at ~1582 cm^{-1}. GP has eight Raman-active modes, the most intense of which is located at 1743.45 cm^{-1} (A$_{1g}$, carbon asymmetric stretching). The PG structure shows eleven Raman-active modes, the most intense of which are located at 1399.15 cm^{-1}
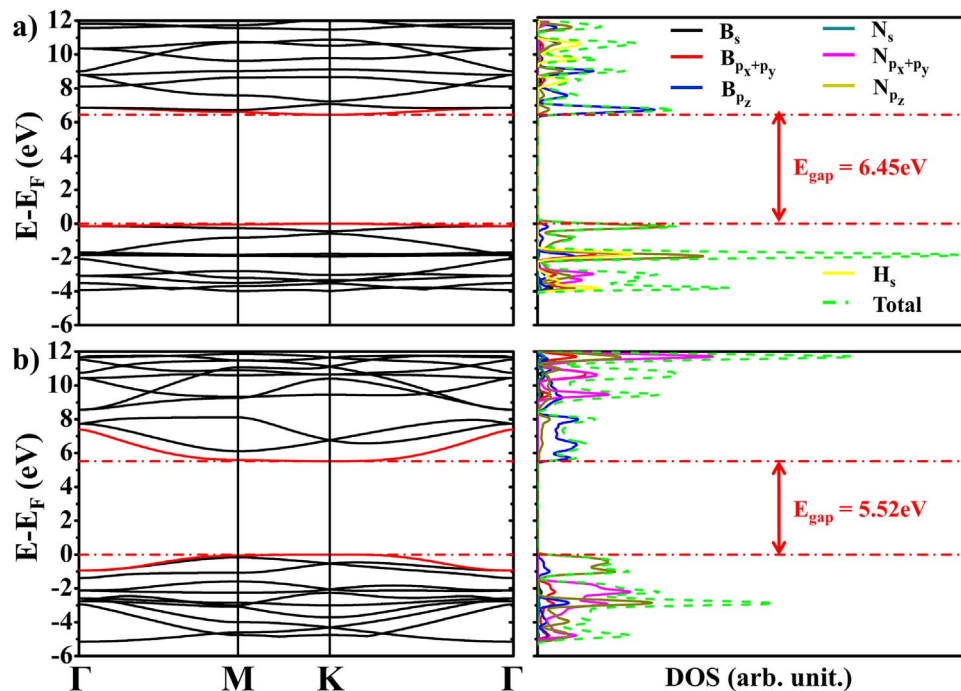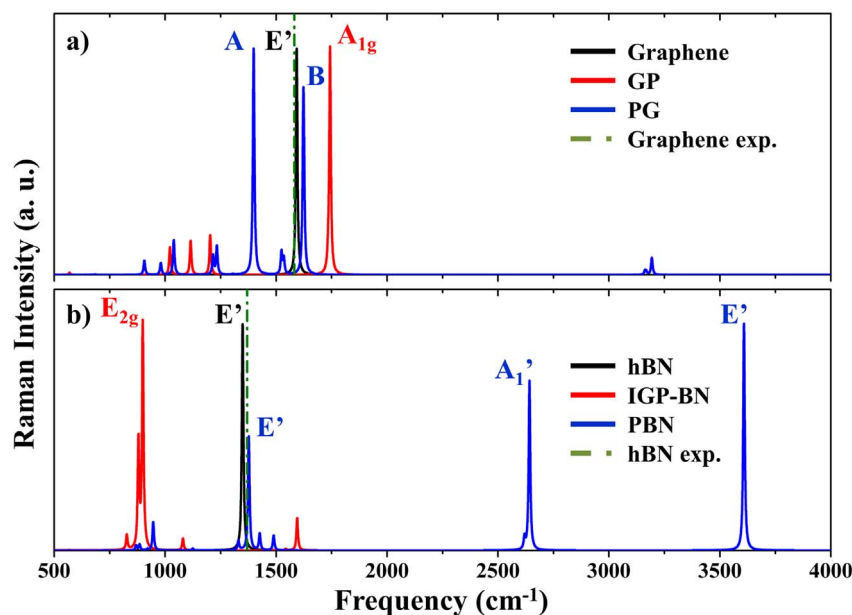

Fig. 3. Band structure and density of states of (a) PBN and (b) IGP-BN.

Fig. 4. Vibrational Raman spectra of (a) graphene (this work and Experimental [67]), GP, and PG; (b) hBN (this work and Experimental [68,69]), IGP-BN, and PBN.

(A, carbon scissoring) and 1622.21 cm^{-1} (B, carbon asymmetric stretching and hydrogen rocking).

The hBN structure presents a single active mode located at 1349.37 cm^{-1} (E', nitrogen and boron scissoring), in good agreement with the peaks in the experimental Raman spectra of two-layer [68] and single-layer [69] hBN films, with frequencies of 1373.40 and ~1369 cm^{-1}, respectively. The IGP-BN structure displays ten Raman-active modes, the most intense of which is located at 899.40 cm^{-1} (E$_{2g}$, boron and nitrogen asymmetric stretching). PBN has eight Raman active modes, the most intense of which are located at 1377.14 cm^{-1} (E', hydrogen rocking and boron/nitrogen asymmetric stretching), 2641.99 cm^{-1} (A$_1$', hydrogen intra-ring symmetric stretching) and 3606.45 cm^{-1} (E', hydrogen intra-ring symmetric stretching).

For both hydrogenated surfaces, PG and PBN, the only vibrational modes active at frequencies above 3000 cm^{-1} are the symmetric and asymmetric stretching of bonds involving hydrogen atoms; the modes below 3000 cm^{-1} are collective vibrations involving all atoms.

3.5. Topological analysis of the electron density (QTAIM)

The QTAIM analysis of PG shown Table 2 highlights the covalent character of the C-C bonds. The C-H bonds, although covalent, present a directional character, i.e., the electron density is shifted towards the H atom, orientating the electron density towards the pore. In this case, the H atoms (exposed towards the pore) are characterized by van der Waals interactions, which increase the electron density in this region.

Fig. 5 displays the Laplacian of the electron density, the BCPs, and the gradient of the electron density for all porous surfaces, showing the trajectory of the charge density. The blue dashed and red solid lines represent depletion and accumulation of charge (negative and positive contours), respectively; Fig. 5a reveals that the trajectory of the electron density is shifted towards the pore region, especially when the density originates from the H atoms, indicating a higher density in this area. It is also interesting to note that the topology of the PG surface is somewhat similar to a hydrogenated benzene ring, as illustrated in Fig. S2 (Supplementary Material).

According to Table S7 (Supplementary Material), all C and H atoms have the same Bader charges (~10^{-5} and 10^{-3} for C and H, respectively) and atomic volumes (~60 and 40 bohr^3 for C and H, respectively): this is a typical characteristic of covalent bonds. Moreover, the atomic charges of atoms located in different planes are slightly more

Table 2

Topological properties of porous surfaces measured at the BCPs: Laplacian of electron density ($\nabla^2\rho(r)$), $|V|/G$ ratio, bond degree ($H/\rho(r)$), ellipticity (ε), and bond type. The "cov", "T", and "vdW" labels denote covalent, transitory and van der Waals bond (interactions) types, respectively.

		$\nabla^2\rho(r)$	$|V|/G$	$H/\rho(r)$	E	bond
PG	C$_8$-H$_3$	−0.983	7.64	−1.02	0.017	cov
	C$_8$-C$_9$	−0.884	4.21	−1.03	0.197	cov
	C$_2$-C$_3$	−0.887	4.20	−1.03	0.198	cov
	C$_7$-C$_{12}$	−0.885	4.22	−1.03	0.193	cov
	C$_{12}$-H$_5$	−0.975	7.64	−1.01	0.018	cov
	C$_{12}$-C$_{11}$	−0.887	4.20	−1.03	0.198	cov
	C$_4$-C$_7$	−0.684	4.72	−0.89	0.084	cov
	H$_6$-H$_5$	0.051	0.83	0.13	0.566	vdW
GP	C$_5$-C$_1$	−0.964	4.01	−1.09	0.250	cov
	C$_1$-C$_4$	−0.739	4.29	−0.94	0.139	cov
	C$_1$-C$_2$	−0.647	4.26	−0.90	0.071	cov
PBN	H$_1$-H$_2$	0.054	0.81	0.13	0.376	vdW
	N$_2$-B$_3$	0.143	1.83	−0.98	0.012	T
	B$_3$-N$_3$	0.280	1.74	−1.00	0.056	T
	B$_2$-H$_1$	−0.376	2.80	−1.14	0.097	cov
	B$_2$-N$_2$	0.260	1.76	−0.99	0.022	T
	N$_3$-H$_2$	−1.58	8.31	−1.35	0.018	cov
IGP-BN	B$_1$-N$_3$	0.356	1.71	−1.01	0.046	T
	B$_1$-N$_2$	0.143	1.83	−0.99	0.037	T
	B$_1$-N$_1$	0.242	1.75	−0.97	0.031	T

positive, as in the case of nonplanar C$_8$ and C$_9$ atoms, although have the same atomic volume of planar atoms.

The BCPs of GP are located at the center of the C-C bonds, i.e., the electron density is uniformly distributed between the two C atoms. The analysis of the Laplacian, V/G, and bond degree ($H/\rho(r)$) shows that all C-C bonds are covalent, which is also confirmed by the elliptical shape of the bonds ($\varepsilon = 1$). Although all bonds had the same character, the C$_5$-C$_1$ bonds in the pore region have a higher electron density, bond degree, and ellipticity than the other bonds, suggesting a more pronounced covalent character, i.e., the electrons are more "arrested", which can have a direct influence on the applications of these materials, such as adsorption of electron-acceptor molecules. As shown in Fig. 5b, "scattered" bonds can be seen along the entire GP structure, even in the vicinity of the pores. The trajectories show that the electron density is distributed closer to the atoms than to the pores, confirming the accumulation of electron density in GP, in contrast with the behavior of PG. As expected for this material, consisting of C atoms and covalent
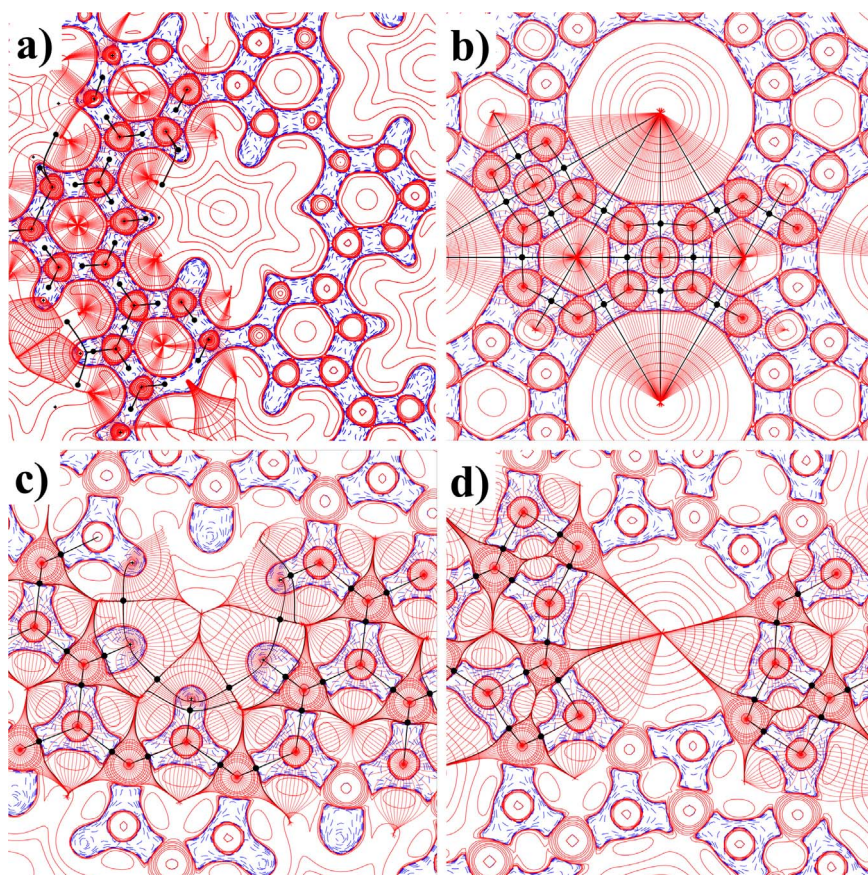
Fig. 5. Laplacian of electron density, BCPs (represented by the black dots), and trajectory of charge density (red lines) for (a) PG, (b) GP, (c) PBN, and (d) IGP-BN surfaces.

bonds, the Bader charges and atomic volumes of all atoms the same, 0.00123 a.u. and 67.45 bohr^3, respectively, i.e., there is no charge transfer between the atoms.

The topological analysis of PBN shows that the B-N bonds are transitory, although they have an accentuated covalent character, as indicated by the negative bond degree ($H/\rho(r) \cong 1$), along with the localization of the BCPs and the low ellipticity value (even though different from zero), which denote directional bonds. The B-H and N-H bonds have covalent character, although the N-H bond seems to be more directional and covalent than the B-H one: this can have direct influence on the B_3-N_3 bonds. As it was observed for PG, PBN there is a weak interaction, a van der Waals type, between the H atoms in the pores. For this reason, both structures present a higher electron density in the pore region than the other materials. Fig. 5c highlights the more directional bonds (due to the proximity of the BCPs of the N atoms) and the electron density depletion in the regions corresponding to the H and B atoms. The higher electron density in the PBN than IGP-BN pores represents an important factor, which can affect and/or enhance the applications of PBN. The analysis of the Bader charges highlights charge depletion for H atoms bonded to N and charge accumulation for H bonded to B. The same conclusion is reached by analyzing the atomic volumes, which increase when H is bonded to B, thus explaining the different charge density trajectories observed for H atoms in Fig. 5c. The B_3 atom, being bonded to two N atoms, presents low charge and atomic volume values, owing to its charge transfer to N atoms.

Finally, in the case of IGP-BN, the bonds exhibit the same behavior observed for PBN, and the topological properties confirm the transitory and strongly covalent character of the B-N bonds. Despite having the same porous geometry of GP, in IGP-BN the electron density is not localized near the B and N atoms, as confirmed by the trajectory of the Laplacian in Fig. 5d, which also highlights a higher electron density in the pores. All B and N atoms have the same Bader charges, 0.179 a.u.,

with different signs, although the N atoms have the largest atomic volume, which indicates charge transfer from B to N. This charge transfer explains the higher density in the pores, in contrast with what observed for the covalent GP material. Further information about BCP distances and charge densities can be found in Table S8 (Supplementary Material).

4. Conclusions

Periodic DFT calculations using BLYP, B3LYP, PBE, PBE0, PBESOL0, HSE06, and modified B3LYP*(12% hybrid) functionals with all-electron TZVP basis sets were performed to simulate the structural, electronic, elastic, and Raman properties of PG, GP, PBN, and IGP-BN single-layers. Among the tested functionals, the B3LYP* yielded the most reliable results, in terms of structural and electronic properties of both bulk graphite and hBN, and for graphene and hBN (0001) single-layer. As the selected functional yield a good description of the precursor structures, they are also expected to predict the properties of PG, GP, PBN, and IGP-BN with good accuracy.

The analysis of the band structure shows that PG and GP presents a indirect band gap between M-K and K points, and a direct band gap located at the K point, respectively. For the PBN and IGP-BN, the inverse behavior was found, as for PBN has a direct band gap, and IGP-BN has an indirect band gap. A significant displacement of the conduction band toward the forbidden region is observed for GP and IGP-BN.

The analysis of the elastic properties indicates that all porous structures are more deformable in the longitudinal direction than their pristine counterparts: the corresponding elastic constants of GP and IGP-BN are around two-thirds of the values measured for their respective precursors. Moreover, GP shows higher rigidity than graphene in the transverse direction. The Young's modulus and Poisson coefficient values exhibit the same trend.

The Raman spectra of graphene and hBN are in good agreement with the experimental results, which allowed us to determine with reliability the Raman spectra of the porous structures and determine their correspondent most intense vibrational modes.

The QTAIM analysis showed that the charge density of the dehydrogenated structures, GP and IGP-BN, is located close to the atoms, whereas that of the hydrogenated PG and PBN materials is shifted towards the pore center, which can directly influence their applications in adsorption processes, among the others. Moreover, PBN, owing to its transitory bonds, has a higher charge density than IGP-BN.

The porous structures examined in this work can play an important role in improving the performance of current and new nanosystems, motivating further experimental and theoretical studies in this field.

Acknowledgements

Appendix A. Supplementary material

Supplementary data associated with this article can be found in the online version at doi:10.1016/j.jssc.2017.10.025.

References

[1] A.K. Geim, K.S. Novoselov, The rise of graphene, Nat. Mater. 6 (2007) 183–191. http://dx.doi.org/10.1038/nmat1849.

[2] D.C. Elias, R.R. Nair, T.M.G. Mohiuddin, S.V. Morozov, P. Blake, M.P. Halsall, A.C. Ferrari, D.W. Boukhvalov, M.I. Katsnelson, A.K. Geim, K.S. Novoselov, Control of Graphene's Properties by Reversible Hydrogenation: evidence for Graphane, Science 323 (2009) 610–613. http://dx.doi.org/10.1126/science.1167130.

[3] Y. Xu, G. Shi, X. Duan, Self-assembled three-dimensional graphene macrostructures: synthesis and applications in supercapacitors, Acc. Chem. Res. 48 (2015) 1666–1675. http://dx.doi.org/10.1021/acs.accounts.5b00117.

[4] Y. Chen, C. Tan, H. Zhang, L. Wang, Two-dimensional graphene analogues for biomedical applications, Chem. Soc. Rev. 44 (2015) 2681–2701. http://dx.doi.org/10.1039/C4CS00300D.

[5] T.R. Fadel, T.M. Fahmy, Immunotherapy applications of carbon nanotubes: from design to safe applications, Trends Biotechnol. 32 (2014) 198–209. http://dx.doi.org/10.1016/j.tibtech.2014.02.005.

[6] Q. Wang, X. Wang, Z. Chai, W. Hu, Low-temperature plasma synthesis of carbon nanotubes and graphene based materials and their fuel cell applications, Chem. Soc. Rev. 42 (2013) 8821–8834. http://dx.doi.org/10.1039/c3cs60205b.

[7] D. Golberg, Y. Bando, Y. Huang, T. Terao, M. Mitome, C. Tang, C. Zhi, Boron Nitride Nanotubes and Nanosheets, ACS Nano 4 (2010) 2979–2993. http://dx.doi.org/10.1021/nn1006495.

[8] C.R. Woods, L. Britnell, A. Eckmann, R.S. Ma, J.C. Lu, H.M. Guo, X. Lin, G.L. Yu, Y. Cao, R.V. Gorbachev, A.V. Kretinin, J. Park, L.A. Ponomarenko, M.I. Katsnelson, Y.N. Gornostyrev, K. Watanabe, T. Taniguchi, C. Casiraghi, H. Gao, A.K. Geim, K.S. Novoselov, Commensurate–incommensurate transition in graphene on hexagonal boron nitride, Nat. Phys. 10 (2014) 1–6. http://dx.doi.org/10.1038/nphys2954.

[9] N.G. Chopra, R.J. Luyken, K. Cherrey, V.H. Crespi, M.L. Cohen, S.G. Louie, A. Zettl, Boron nitride nanotubes, Science 269 (1995) 966–967. http://dx.doi.org/10.1126/science.269.5226.966.

[10] D. Golberg, Y. Bando, O. Stéphan, K. Kurashima, Octahedral boron nitride fullerenes formed by electron beam irradiation, Appl. Phys. Lett. 73 (1998) 2441. http://dx.doi.org/10.1063/1.122475.

[11] X. Li, X. Hao, M. Zhao, Y. Wu, J. Yang, Y. Tian, G. Qian, Exfoliation of Hexagonal Boron Nitride by Molten Hydroxides, Adv. Mater. 25 (2013) 2200–2204. http://dx.doi.org/10.1002/adma.201204031.

[12] R. Quhe, J. Ma, Z. Zeng, K. Tang, J. Zheng, Y. Wang, Z. Ni, L. Wang, Z. Gao, J. Shi, J. Lu, Tunable band gap in few-layer graphene by surface adsorption, Sci. Rep. 3 (2013) 1794. http://dx.doi.org/10.1038/srep01794.

[13] R. Paupitz, P.A.S. Autreto, S.B. Legoas, S.G. Srinivasan, A.C.T. van Duin, D.S. Galvao, Graphene to fluorographene and fluorographane: a theoretical study,

[14] S. Stankovich, D.A. Dikin, R.D. Piner, K.A. Kohlhaas, A. Kleinhammes, Y. Jia, Y. Wu, S.T. Nguyen, R.S. Ruoff, Synthesis of graphene-based nanosheets via chemical reduction of exfoliated graphite oxide, Carbon 45 (2007) 1558–1565. http://dx.doi.org/10.1016/j.carbon.2007.02.034.

[15] M.Z.S. Flores, P.A.S. Autreto, S.B. Legoas, D.S. Galvao, Graphene to graphane: a theoretical study, Nanotechnology 20 (2009) 465704. http://dx.doi.org/10.1088/0957-4484/20/46/465704.

[16] Z.H. Ni, T. Yu, Y.H. Lu, Y.Y. Wang, Y.P. Feng, Z.X. Shen, Uniaxial strain on graphene: Raman spectroscopy study and band-gap opening, ACS Nano 2 (2008) 2301–2305. http://dx.doi.org/10.1021/nn800459e.

[17] F. Banhart, J. Kotakoski, A.V. Krasheninnikov, Structural defects in graphene, ACS Nano 5 (2011) 26–41. http://dx.doi.org/10.1021/nn102598m.

[18] G. Giovannetti, P.A. Khomyakov, G. Brocks, V.M. Karpan, J. Van Den Brink, P.J. Kelly, Doping graphene with metal contacts, Phys. Rev. Lett. 101 (2008) 4–7. http://dx.doi.org/10.1103/PhysRevLett.101.026803.

[19] M. Bieri, M. Treier, J. Cai, K. Aït-Mansour, P. Ruffieux, O. Gröning, P. Gröning, M. Kastler, R. Rieger, X. Feng, K. Müllen, R. Fasel, Porous graphenes: two-dimensional polymer synthesis with atomic precision, Chem. Commun. (2009) 6919. http://dx.doi.org/10.1039/b915190g.

[20] Y. Li, Z. Zhou, P. Shen, Z. Chen, Two-dimensional polyphenylene: experimentally available porous graphene as a hydrogen purification membrane, Chem. Commun. 46 (2010) 3672. http://dx.doi.org/10.1039/b926313f.

[21] A. Du, Z. Zhu, S.C. Smith, Multifunctional porous graphene for nanoelectronics and hydrogen storage: new properties revealed by first principle calculations, J. Am. Chem. Soc. 132 (2010) 2876–2877. http://dx.doi.org/10.1021/ja100156d.

[22] Y. Ding, Y. Wang, S. Shi, W. Tang, Electronic structures of porous graphene, BN, and BC2N sheets with one- and two-hydrogen passivations from first principles, J. Phys. Chem. C 115 (2011) 5334–5343. http://dx.doi.org/10.1021/jp110336r.

[23] G. Brunetto, P.A.S. Autreto, L.D. Machado, B.I. Santos, R.P.B. Dos Santos, D.S. Galvão, Nonzero gap two-dimensional carbon allotrope from porous graphene, J. Phys. Chem. C 116 (2012) 12810–12813. http://dx.doi.org/10.1021/jp211300n.

[24] M. Elstner, D. Porezag, G. Jungnickel, J. Elsner, M. Haugk, T. Frauenheim, S. Suhai, G. Seifert, Self-consistent-charge density-functional tight-binding method for simulations of complex materials properties, Phys. Rev. B 58 (1998) 7260–7268. http://dx.doi.org/10.1103/PhysRevB.58.7260.

[25] Y.X. Yu, Graphenylene: a promising anode material for lithium-ion batteries with high mobility and storage, J. Mater. Chem. A 1 (2013) 13559. http://dx.doi.org/10.1039/c3ta12639k.

[26] Q. Song, B. Wang, K. Deng, X. Feng, M. Wagner, J.D. Gale, K. Müllen, L. Zhi, M. Saleh, X.L. Feng, K. Müllen, R. Fasel, Graphenylene, a unique two-dimensional carbon network with nondelocalized cyclohexatriene units, J. Mater. Chem. C 1 (2013) 38–41. http://dx.doi.org/10.1039/C2TC00006G.

[27] R. Totani, C. Grazioli, T. Zhang, I. Bidermane, J. Lüder, M. de Simone, M. Coreno, B. Brena, L. Lozzi, C. Puglia, Electronic structure investigation of biphenylene films, J. Chem. Phys. 146 (2017) 54705. http://dx.doi.org/10.1063/1.4975104.

[28] Q.S. Du, P.D. Tang, H.L. Huang, F.L. Du, K. Huang, N.Z. Xie, S.Y. Long, Y.M. Li, J.S. Qiu, R.B. Huang, A new type of two-dimensional carbon crystal prepared from 1,3,5-trihydroxybenzene, Sci. Rep. 7 (2017) 40796. http://dx.doi.org/10.1038/srep40796.

[29] E. Perim, R. Paupitz, P.A.S. Autreto, D.S. Galvao, Inorganic Graphenylene: a Porous Two-Dimensional Material With Tunable Band Gap, J. Phys. Chem. C 118 (2014) 23670–23674. http://dx.doi.org/10.1021/jp502119y.

[30] R.F.W. Bader, Atoms in Molecules: A Quantum Theory (International Series of Monographs on Chemistry), Oxford University Press, UK, 1990.

[31] C. Gatti, S. Casassa, TOPOND User's Manual, CNR-CSRSRC, Milano, 2013.

[32] R. Dovesi, R. Orlando, A. Erba, C.M. Zicovich-Wilson, B. Civalleri, S. Casassa, L. Maschio, M. Ferrabone, M. De La Pierre, P. D'Arco, Y. Noël, M. Causà, M. Rérat, B. Kirtman, CRYSTAL14: a program for the *ab initio* investigation of crystalline solids, Int. J. Quantum Chem. 114 (2014) 1287–1317. http://dx.doi.org/10.1002/qua.24658.

[33] M. C, Y.N.R. Dovesi, V.R. Saunders, C. Roetti, R. Orlando, C.M. Zicovich-Wilson, F. Pascale, B. Civalleri, K. Doll, N.M. Harrison, I.J. Bush, P. D'Arco, M. Llunell, CRYSTAL14 User's Manual, University of Torino, Torino, 2014.

[34] M.F. Peintinger, D.V. Oliveira, T. Bredow, Consistent Gaussian basis sets of triple-zeta valence with polarization quality for solid-state calculations, J. Comput. Chem. 34 (2013) 451–459. http://dx.doi.org/10.1002/jcc.23153.

[35] S. Casassa, A. Erba, J. Baima, R. Orlando, Electron density analysis of large (molecular and periodic) systems: a parallel implementation, J. Comput. Chem. 36 (2015) 1940–1946. http://dx.doi.org/10.1002/jcc.24033.

[36] P.L.A. Popelier, A robust algorithm to locate automatically all types of critical points in the charge density and its Laplacian, Chem. Phys. Lett. 228 (1994) 160–164. http://dx.doi.org/10.1016/0009-2614(94)00897-3.

[37] R.W.G. Wyckoff, , 2ednCrystal Structures 1, Interscience, New York, 1963.

[38] R.S. Pease, An X-ray study of boron nitride, Acta Crystallogr. 5 (1952) 356–361. http://dx.doi.org/10.1107/S0365110X52001064.

[39] G. Cassabois, P. Valvin, B. Gil, Hexagonal boron nitride is an indirect bandgap semiconductor, Nat. Photonics 10 (2016) 262–267. http://dx.doi.org/10.1038/nphoton.2015.277.

[40] D.R. Cooper, B. D'Anjou, N. Ghattamaneni, B. Harack, M. Hilke, A. Horth, N. Majlis, M. Massicotte, L. Vandsburger, E. Whiteway, V. Yu, Experimental Review of Graphene, ISRN, Condens. Matter Phys. 2012 (2012) 1–56. http://dx.doi.org/10.5402/2012/501686.

[41] Y. Stehle, H.M. Meyer, R.R. Unocic, M. Kidder, G. Polizos, P.G. Datskos, R. Jackson, S.N. Smirnov, I.V. Vlassiouk, Synthesis of hexagonal boron nitride

monolayer: control of nucleation and crystal morphology, Chem. Mater. 27 (2015) 8041–8047. http://dx.doi.org/10.1021/acs.chemmater.5b03607.

[42] N.L. Marana, S. Casassa, E. Longo, J.R. Sambrano, Structural, electronic, vibrational, and topological analysis of single-walled zinc oxide nanotubes, J. Phys. Chem. C 120 (2016) 6814–6823. http://dx.doi.org/10.1021/acs.jpcc.5b11905.

[43] N.L. Marana, A.R. Albuquerque, F.A. La Porta, E. Longo, J.R. Sambrano, Periodic density functional theory study of structural and electronic properties of single-walled zinc oxide and carbon nanotubes, J. Solid State Chem. 237 (2016) 36–47. http://dx.doi.org/10.1016/j.jssc.2016.01.017.

[44] A. Beltrán, J. Andrés, J.R. Sambrano, E. Longo, Density Functional Theory Study on the Structural and Electronic Properties of Low Index Rutile Surfaces for TiO 2 /SnO 2 /TiO 2 and SnO 2 /TiO 2 /SnO 2 Composite Systems †, J. Phys. Chem. A 112 (2008) 8943–8952. http://dx.doi.org/10.1021/jp801604n.

[45] M.L. Moreira, E.C. Paris, G.S. do Nascimento, V.M. Longo, J.R. Sambrano, V.R. Mastelaro, M.I.B. Bernardi, J. Andrés, J.A. Varela, E. Longo, Structural and optical properties of CaTiO3 perovskite-based materials obtained by microwave-assisted hydrothermal synthesis: an experimental and theoretical insight, Acta Mater. 57 (2009) 5174–5185. http://dx.doi.org/10.1016/j.actamat.2009.07.019.

[46] A.R. Albuquerque, M.L. Garzim, I.M.G. dos Santos, V. Longo, E. Longo, J.R. Sambrano, DFT Study with Inclusion of the Grimme Potential on Anatase TiO 2: structure, Electronic, and Vibrational Analyses, J. Phys. Chem. A 116 (2012) 11731–11735. http://dx.doi.org/10.1021/jp308318j.

[47] V.L. Solozhenko, A.G. Lazarenko, J.P. Petitet, A.V. Kanaev, Bandgap energy of graphite-like hexagonal boron nitride, J. Phys. Chem. Solids 62 (2001) 1331–1334. http://dx.doi.org/10.1016/S0022-3697(01)00030-0.

[48] Y.-N. Xu, W.Y. Ching, Calculation of ground-state and optical properties of boron nitrides in the hexagonal, cubic, and wurtzite structures, Phys. Rev. B 44 (1991) 7787–7798. http://dx.doi.org/10.1103/PhysRevB.44.7787.

[49] J. Furthmüller, J. Hafner, G. Kresse, *Ab initio* calculation of the structural and electronic properties of carbon and boron nitride using ultrasoft pseudopotentials, Phys. Rev. B 50 (1994) 15606–15622. http://dx.doi.org/10.1103/PhysRevB.50.15606.

[50] X. Blase, A. Rubio, S.G. Louie, M.L. Cohen, Quasiparticle band structure of bulk hexagonal boron nitride and related systems, Phys. Rev. B 51 (1995) 6868–6875. http://dx.doi.org/10.1103/PhysRevB.51.6868.

[51] B. Arnaud, S. Lebègue, P. Rabiller, M. Alouani, Huge Excitonic Effects in Layered Hexagonal Boron Nitride, Phys. Rev. Lett. 96 (2006) 26402. http://dx.doi.org/10.1103/PhysRevLett.96.026402.

[52] S.-P. Gao, Crystal structures and band gap characters of h-BN polytypes predicted by the dispersion corrected DFT and GW method, Solid State Commun. 152 (2012) 1817–1820. http://dx.doi.org/10.1016/j.ssc.2012.07.022.

[53] K. Watanabe, T. Taniguchi, H. Kanda, Direct-bandgap properties and evidence for ultraviolet lasing of hexagonal boron nitride single crystal, Nat. Mater. 3 (2004) 404–409. http://dx.doi.org/10.1038/nmat1134.

[54] A. Zunger, A. Katzir, A. Halperin, Optical properties of hexagonal boron nitride, Phys. Rev. B 13 (1976) 5560–5573. http://dx.doi.org/10.1103/PhysRevB.13.5560.

[55] D.A. Evans, A.G. McGlynn, B.M. Towlson, M. Gunn, D. Jones, T.E. Jenkins, R. Winter, N.R.J. Poolton, Determination of the optical band-gap energy of cubic

and hexagonal boron nitride using luminescence excitation spectroscopy, J. Phys. Condens. Matter 20 (2008) 75233. http://dx.doi.org/10.1088/0953-8984/20/7/075233.

[56] C. Lee, X. Wei, J.W. Kysar, J. Hone, Measurement of the elastic properties and intrinsic strength of monolayer graphene, Science 321 (2008) 385–388. http://dx.doi.org/10.1126/science.1157996.

[57] O.L. Blakslee, D.G. Proctor, E.J. Seldin, G.B. Spence, T. Weng, Elastic constants of compression-annealed pyrolytic graphite, J. Appl. Phys. 41 (1970) 3373–3382. http://dx.doi.org/10.1063/1.1659428.

[58] E.J. Seldin, C.W. Nezbeda, Elastic constants and electron-microscope observations of neutron-irradiated compression-annealed pyrolytic and single-crystal graphite, J. Appl. Phys. 41 (1970) 3389–3400. http://dx.doi.org/10.1063/1.1659430.

[59] K.N. Kudin, G.E. Scuseria, B.I. Yakobson, C2F, BN, and C nanoshell elasticity from ab initio computations, Phys. Rev. B 64 (2001) 235406. http://dx.doi.org/10.1103/PhysRevB.64.235406.

[60] P.M. Anderson, J.P. Hirth, J. Lothe, Theory of Dislocations, 3rd edn., Cambridge University Press, 2017.

[61] A.R. Albuquerque, J. Maul, E. Longo, I.M.G. Dos Santos, J.R. Sambrano, Hydrostatic and [001] uniaxial pressure on anatase TiO2 by periodic B3LYP-D* calculations, J. Phys. Chem. C 117 (2013) 7050–7061. http://dx.doi.org/10.1021/jp311572y.

[62] J. Maul, I.M.G. Santos, J.R. Sambrano, A. Erba, Thermal properties of the orthorhombic CaSnO3 perovskite under pressure from ab initio quasi-harmonic calculations, Theor. Chem. Acc. 135 (2016) 36. http://dx.doi.org/10.1007/s00214-015-1765-9.

[63] J. Bai, X. Zhong, S. Jiang, Y. Huang, X. Duan, Graphene nanomesh, Nat. Nanotechnol. 5 (2010) 190–194. http://dx.doi.org/10.1038/nnano.2010.8.

[64] M. Ferrero, M. Rérat, B. Kirtman, R. Dovesi, Calculation of first and second static hyperpolarizabilities of one- to three-dimensional periodic compounds. Implementation in the CRYSTAL code, J. Chem. Phys. 129 (2008) 244110. http://dx.doi.org/10.1063/1.3043366.

[65] M. Ferrero, M. Rérat, R. Orlando, R. Dovesi, The calculation of static polarizabilities of 1-3D periodic compounds. the implementation in the crystal code, J. Comput. Chem. 29 (2008) 1450–1459. http://dx.doi.org/10.1002/jcc.20905.

[66] M. Ferrero, M. Rérat, R. Orlando, R. Dovesi, Coupled perturbed Hartree-Fock for periodic systems: the role of symmetry and related computational aspects, J. Chem. Phys. 128 (2008) 14110. http://dx.doi.org/10.1063/1.2817596.

[67] M.S. Dresselhaus, A. Jorio, M. Hofmann, G. Dresselhaus, R. Saito, Perspectives on carbon nanotubes and graphene Raman spectroscopy, Nano Lett. 10 (2010) 751–758. http://dx.doi.org/10.1021/nl904286r.

[68] L. Song, L. Ci, H. Lu, P.B. Sorokin, C. Jin, J. Ni, A.G. Kvashnin, D.G. Kvashnin, J. Lou, B.I. Yakobson, P.M. Ajayan, Large Scale Growth and Characterization of Atomic Hexagonal Boron Nitride Layers, Nano Lett. 10 (2010) 3209–3215. http://dx.doi.org/10.1021/nl1022139.

[69] R.V. Gorbachev, I. Riaz, R.R. Nair, R. Jalil, L. Britnell, B.D. Belle, E.W. Hill, K.S. Novoselov, K. Watanabe, T. Taniguchi, A.K. Geim, P. Blake, Hunting for monolayer boron nitride: optical and Raman signatures, Small 7 (2011) 465–468. http://dx.doi.org/10.1002/smll.201001628.